J. Fluid Mech. (2007), *vol.* 586, *pp.* 423–448. © 2007 Cambridge University Press
doi:10.1017/S002211200700729X Printed in the United Kingdom

Oscillatory instability and rupture in a thin melt film on its crystal subject to freezing and melting

M. BEERMAN AND L. N. BRUSH

Department of Materials Science and Engineering, University of Washington, Seattle, WA 98195, USA

(Received 24 August 2006 and in revised form 18 April 2007)

Lubrication theory is used to derive a coupled pair of strongly nonlinear partial differential equations governing the evolution of interfaces separating a thin film of a pure melt from its crystalline phase and from a gas. The free melt–gas (MG) interface deforms in response to the local state of stress and the crystal–melt (CM) interface can deform by freezing and melting only. A linear stability analysis of a static, uniform film subject to the effects of MG interface capillary forces, thermocapillary forces, the latent heat of fusion, van der Waals attraction, heat transfer and solidification volume change effects, reveals stationary and oscillatory instabilities. The effect of a temperature gradient (by increasing the gas phase temperature) is to stabilize a film. As the temperature gradient is *reduced*, the onset of instability is oscillatory and is at a unique, finite wavenumber. Instability is oscillatory for all marginally stable, non-isothermal cases. Crystals with higher density than the melt are more stable, whereas crystals with lower density are less stable in the presence of an applied temperature gradient. Fully nonlinear numerical solutions show that oscillatory instabilities lead to rupture by growth of standing or travelling waves. Rupture times and the number of oscillations to rupture increase as the temperature gradient is increased. For stationary linearly unstable initial conditions, the CM interface retreats by melting away from the tip region of the encroaching MG interface due to a rise in the heat flux there as the film thins and nears rupture. Larger amplitude disturbances increase the maximum allowable temperature for instability, at a given wavenumber, and decrease the time to rupture at fixed temperature and wavenumber.

1. Introduction

Understanding the stability and morphological evolution of thin liquid films is vital for a variety of applications such as processing of foam networks (Ashby *et al.* 2000; Banhart 2001), pulsed laser micromachining (Ajaev & Willis 2006) and liquid multilayers (Fisher & Golovin 2005). For example, in a foam, there are sections of crowded gas bubbles separated by uniform, thin, liquid lamella. One possible method for freezing a metallic foam is directional solidification by pulling it through a controlled, unidirectional thermal gradient. The lamella between bubbles may be oriented in any direction relative to the applied temperature gradient, including an orientation perpendicular to the axial direction of a lamella. In laser applications, heat sources are applied atop crystalline materials, resulting in very thin liquid films which may then resolidify. In this study, we examine the dynamics of a very thin liquid film, such as a partially frozen lamella, with a temperature gradient oriented perpendicular

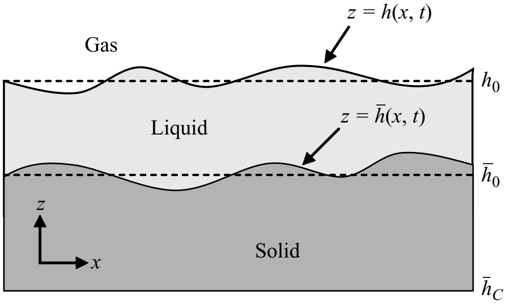

FIGURE 1. A two-dimensional thin melt film is bounded by melt–gas ($h(x, t)$) and crystal–melt ($\bar{h}(x, t)$) interfaces. Dashed lines h_0 and $\bar{h}_0$ represent a uniformly thick melt layer which is used as a base state in a linear stability analysis. The crystal is a layer with a temperature gradient applied at $z = \bar{h}_C$.

to the axial direction of the film. This corresponds to those cases described above; however, the results of this study are relevant for any thin metallic film in contact with its non-premelting (usually close-packed) crystalline interface.

The chosen configuration allows for careful benchmarking of the results with previous studies of the rupture of liquid films atop non-deformable, inert substrates. The comparisons are necessary in order to understand how a thermal gradient coupled with an additional crystal–melt interface, deformable by melting or freezing, affects rupture dynamics. For the results presented in this work, the properties of aluminium are used, since these are well studied, and it has potential use in many applications (Banhart 2001).

The general three-phase solidification geometry applicable in the examples discussed above is shown in figure 1. The system consists of a solid layer, a thin liquid film (the melt of the crystal) and an inert gas phase. The unique aspect of this configuration is the presence of a crystal-melt interface which can deform, potentially leading to a rich array of patterns. The thin film configuration leads to fluid dynamics controlled by melt–gas (MG) interfacial phenomena, solidification phenomena and viscous effects. Intermolecular forces also become significant for films that are sufficiently thin, as in the examples listed above. In comparison to bulk multiphase systems, the combination of thinness of the geometry and the additional forces leads to unique dynamics.

It has been well established that in a thin, pure, liquid layer on a solid substrate, fluid flow depends heavily on viscous forces and surface tension. Based on experimental observations, Sheludko (1967) proposed that long-range intermolecular forces, due to London dispersion or van der Waals attraction, give rise to instability of ultra-thin (100—1000 Å) liquid layers, ultimately leading to rupture. Ruckenstein & Jain (1974) accounted for this dispersion force by incorporating it into the pressure term of the Navier–Stokes equations that govern fluid flow in the film. They showed that there exists a critical surface perturbation wavelength λ_C that is much larger than the film thickness, below (above) which the film is stable (unstable). They predicted a time to rupture t_R based on the linear growth rate of a perturbation of critical wavelength.

Williams & Davis (1982) derived a strongly nonlinear evolution equation for the interface shape of a thin film on a substrate in the lubrication limit. They formalized the critical wavelength result from Ruckenstein & Jain, and developed a long-wave theory of the thin film in which the fluid flow equations and boundary conditions are written as a regular perturbation series in terms of the ratio of the film thickness to a characteristic lateral length scale in the film. Numerical solutions of the fully nonlinear governing equation for the shape showed that the nonlinear effects speed up the time to rupture compared to the estimate given by the linear theory.

VanHook *et al.* (1995) identified a long-wave instability for the case of surface-tension-driven Bénard convection on a substrate. Below a critical thickness, the primary instability is long-wave, which leads to dewetting over large regions of the substrate. Above the critical thickness, hexagonal convection cells are the primary instability. The experimental results were compared to long-wave theory and linear analysis, and were generalized for microgravity environments.

Burelbach, Bankoff & Davis (1988) utilized long-wave theory to derive evolution equations for interface shapes under isothermal and non-isothermal conditions, allowing for evaporation and condensation at the liquid–gas interface. They also investigated the apparent singularity of the gas–liquid interface near a protuberance tip as it nears rupture, and have derived similarity solutions for the tip region at times very close to t_R. Near rupture, similarity solutions for a gas–liquid interface bounding a thin liquid film on a solid substrate are also derived by Zhang & Lister (1999). They conclude that there is a countably infinite set of similarity solutions in which the film thickness decreases as $(t_R - t)^{1/5}$ where $(t_R - t)$ is the time remaining until rupture.

Erneaux & Davis (1992) considered the case of a free liquid film bounded by two liquid–gas interfaces under isothermal conditions. Long-wave asymptotic theory is applied and a pair of coupled nonlinear equations governing the evolution of the two bounding surfaces is derived. They obtain an estimate for the rupture time based on the nonlinear theory. An excellent review on the dynamics of thin films is provided by Oron, Davis & Bankoff (1997), for a very wide range of conditions.

Bandyopadhyay, Gulabani & Sharma (2005) investigated interfacial instability of thin bilayers of immiscible fluids on a solid substrate. They applied lubrication theory to determine linear growth rates as a function of viscosity and layer thickness for several material systems that are of relevance to integrated circuit technology. They also numerically simulate the nonlinear morphological evolution. Fisher & Golovin (2005) recently derived a system of strongly nonlinear evolution equations governing the dynamics of a two-layer liquid system on a solid substrate including surfactants at liquid–liquid interfaces. Analysis showed the appearance of oscillatory instability leading to standing or travelling waves.

Often thin melt films will appear between a crystal and a vapour near, but below, the bulk melting point of the material. This phenomenon is known as premelting of free surface layers. Premelting has significant macroscopic consequences, and contributes to environmental effects such as frost heave and glacier flow (Dash, Fu & Wettlaufer 1995). Dash *et al.* have shown how the premelted film thickness depends on the reduced temperature $(T_m - T)/T_m$ (where $T < T_m$), the molecular potential and surface energy. Wettlaufer *et al.* (1996) and Wettlaufer, Worster & Wilen (1997) have investigated many cases of flows in premelted thin films, and have considered a large variety of physical effects that drive the interfacial evolution and melting/freezing of the CM interface in these systems. (See the recent article by Wettlaufer & Worster (2006) and references therein.)

The causes of the premelting of surfaces and the forces leading to rupture of thin liquid films are related to the intermolecular potentials arising within the surface layers separating the phases, such as the long-range van der Waals forces. The intermolecular potentials giving rise to these forces vary with interface geometry and material dielectric function (Israelachvili 1991) and one result is that they give rise to a difference in pressure in a thin film compared with its bulk state, referred to as the disjoining pressure. Positive disjoining pressure can lead to spontaneous thickening of a film, a negative disjoining pressure can lead to thinning and instability of a thin liquid layer. Theoretical estimates of the material-dependent Hamaker constant, a measure of the strength of the disjoining pressure, have been found for a variety of solid phases bounding thin films of water (Wilen *et al.* 1995). Molecular dynamic studies (Tartaglino *et al.* 2005) and ion shadowing and blocking experiments (Pluis *et al.* 1987; Frenken & van der Veen 1985) of melting and non-melting on solid surfaces suggest that many metal crystal facets, such as Pb(110) (Pluis *et al.* 1989) exhibit surface melting. However, close-packed crystal facets, such as Al(111) and Pb(111) (Pluis *et al.* 1987) are non-melting and can even survive surface overheating. Whether or not a surface has a stabilizing or destabilizing dispersion force depends on the sign of the Hamaker constant (Dash *et al.* 1995; Tartaglino *et al.* 2005). In this analysis, premelted films are not considered.

In the present paper, we use lubrication theory to derive appropriate governing equations for a thin film subject to a non-uniform temperature and in which both the melt–gas and the crystal—melt interfaces bounding the film are deformable. The model is used to study the instability and evolution to a point near rupture of the thin film. In the following sections, the governing equations for the three-phase system are presented (shown in figure 1). These are then rescaled and a pair of coupled evolution equations are derived. A linear stability analysis of a uniform film reveals the effect of the thermal field and solidification phenomenon on stability. Numerical results reveal a rich variety of nonlinear behaviours, leading to rupture.

2. Governing equations

In two dimensions, the Navier–Stokes and continuity equations govern the components of the fluid velocity $u(x, z, t)$, $w(x, z, t)$ and pressure $p(x, z, t)$:

$$\rho^l(u_t + uu_x + wu_z) = -p^*_x + \mu(u_{xx} + u_{zz}), \tag{2.1}$$

$$\rho^l(w_t + uw_x + ww_z) = -p^*_z + \mu(w_{xx} + w_{zz}), \tag{2.2}$$

and

$$u_x + w_z = 0, \tag{2.3}$$

where subscripts x and z denote partial derivatives, ρ^l is the melt density and μ is the melt viscosity. The effective pressure $p^* = p + \phi$ is defined where long-range van der Waals molecular interactions are included in ϕ (gravity is negligible). Disjoining pressures in thin films arise due to various molecular interactions including van der Waals, electrostatic and structural forces (Chernov & Temkin 1976), which may be attractive and/or repulsive, short-range and/or long-range. (Some examples are discussed in Oron *et al.* 1997.) As a film approaches rupture, repulsive forces can play an increasing role (Kao, Golovin & Davis 2006). However, in this study we are only concerned with the long-range attractive van der Waals forces, since these drive the instability of a film, and so we neglect the repulsive forces. As a result, we employ the form $\phi = (A'/6\pi)(h - \overline{h})^{-3}$ to represent the intermolecular interactions, where A' is the Hamaker constant. This form is valid for parallel or quasi-parallel interfaces (Davis 2000), and is the same used in many previous studies including Williams & Davis (1982).

Recently, Wu & Wong (2004) have derived a disjoining pressure that depends on the slope and the curvature of a film which makes a contact angle/line at the surface of a solid substrate. This form of the disjoining pressure, among other effects, keeps a contact line from moving without slip. However, the effects of a slope-dependent disjoining pressure would appear at higher order in a linear analysis of a uniform film (given in the following section). In addition, this study involves film evolution up to the point of rupture, prior to contact line formation. Therefore, the slope-dependent disjoining pressure is not included in this study.

In a non-isothermal system the melt temperature T^l is governed by

$$\rho^l c^l \left(T^l_t + u T^l_x + w T^l_z\right) = k^l \left(T^l_{xx} + T^l_{zz}\right), \tag{2.4}$$

and the crystal temperature T^s obeys

$$\rho^s c^s \left(T^s_t + u T^s_x + w T^s_z\right) = k^s \left(T^s_{xx} + T^s_{zz}\right), \tag{2.5}$$

where c^l (c^s) is the heat capacity of the melt (crystal), k^l (k^s) is the thermal conductivity of the melt (crystal) and ρ^s is the density of the crystal.

At the MG interface $z = h(x, t)$, the kinematic condition is

$$w = h_t + u h_x, \tag{2.6}$$

where the components of the fluid velocity are evaluated at the interface; i.e. $u = u(h(x, t), x, t)$ and $w = w(h(x, t), x, t)$. The condition on the normal component of stress at the interface is

$$-p^* + \phi + p^g + \frac{2\mu}{\left(1 + h_x^2\right)}\left[\left(u_x h_x^2 + w_z\right) - h_x(u_z + w_x)\right] = \gamma^{MG} \frac{h_{xx}}{\left(1 + h_x^2\right)^{3/2}}, \tag{2.7}$$

where p^g is the hydrostatic pressure in the inviscid gas phase. The right-hand side of (2.7) is the product of the MG surface energy γ^{MG} and the curvature of the interface.

The tangential component of the shear stress at the interface is balanced by the thermo-capillary force per unit area:

$$-2\mu(u_x - w_z)h_x + \mu(u_z + w_x)\left(1 - h_x^2\right) = \gamma_x^{MG}(1 + h_x^2)^{1/2}. \tag{2.8}$$

The right-hand side represents thermocapillary or thermal Marangoni effects, operative when the surface tension depends on temperature (e.g. Wheeler 1993),

$$\gamma^{MG}(T^l) = \gamma_0^{MG} - \gamma_T^{MG}(T^l - T_0), \tag{2.9}$$

where γ_T^{MG} is the rate of change of the surface energy γ^{MG} with respect to temperature and is given as a material property; γ_0^{MG} is a reference value of surface energy evaluated at T_0.

The heat flux into the melt layer at the MG interface is balanced by 'convective' heat transfer from the gas

$$-k^l(\nabla T^l \cdot \hat{\boldsymbol{n}}) = \alpha_{Th}(T^l - T_\infty), \tag{2.10}$$

where α_{Th} is an empirical heat transfer coefficient and $\hat{n} = (-h_x \hat{\boldsymbol{i}} + \hat{\boldsymbol{k}})(1 + h_x^2)^{-1/2}$ is the unit vector normal to the MG interface pointing into the gas phase. T_∞ is a prescribed ambient gas temperature and is a control parameter. In addition, the temperature is continuous at all interfaces.

The CM interface, $z = \overline{h}(x, t)$, has unit normal vector $\hat{\overline{\boldsymbol{n}}} = (-\overline{h}_x \hat{\boldsymbol{i}} + \hat{\boldsymbol{k}})(1 + \overline{h}_x^2)^{-1/2}$ pointing into the melt, a unit tangent vector $\hat{\overline{\boldsymbol{t}}} = (\hat{\boldsymbol{i}} + \overline{h}_x \hat{\boldsymbol{k}})(1 + \overline{h}_x^2)^{-1/2}$ and a local normal growth speed $\hat{\overline{\boldsymbol{v}}}_n = \overline{h}_t(1 + \overline{h}_x^2)^{-1/2}$. At the CM interface, there is the no-slip condition $\boldsymbol{u} \cdot \hat{\overline{\boldsymbol{t}}} = 0$, where $\boldsymbol{u} = (u, w)$ is the fluid velocity.

The equilibrium crystal–melt interface temperature is given by the Gibbs–Thomson condition

$$T_I^l = T_M - \frac{T_M\left(\gamma^{CM} + \gamma^{CM}_{\phi\phi}\right)}{L_v}\overline{K}, \tag{2.11}$$

where T_M is the melting point of the pure bulk crystal (planar interface), L_v is the latent heat of fusion per unit volume of crystal phase, γ^{CM} is the CM interfacial energy, and the subscripts ϕ denote differentiation with respect to the angle the normal vector makes with the interface. For isotropic crystals $\gamma^{CM}_{\phi\phi}$ is zero. Here, the CM curvature $\overline{K}$ is positive for a crystal sphere.

Evolution of the CM interface results in solidification shrinkage/expansion so that:

$$\frac{\rho^l - \rho^s}{\rho^l}\overline{v}_n = \boldsymbol{u}\cdot\hat{\overline{\boldsymbol{n}}}. \tag{2.12}$$

Equation (2.8) indicates that solidification shrinkage promotes normal flow towards the CM interface (e.g. Al), whereas solidification expansion promotes flow away from the interface (e.g. ice). Finally, at the CM interface, the difference in the heat fluxes is balanced by the rate of latent heat evolved per unit time and per unit area of interface during growth:

$$L_v\overline{v}_n = -k^l\nabla T^l\cdot\hat{\overline{\boldsymbol{n}}} + k^s\nabla T^s\cdot\hat{\overline{\boldsymbol{n}}}. \tag{2.13}$$

In this work, the crystal may be assumed to be a layer of thickness $\overline{h}_C$. At $z=-\overline{h}_C$ the z-component of the applied temperature gradient is held constant, $\nabla\boldsymbol{T}\cdot\hat{\boldsymbol{k}} = G_L^{app}$, where G_L^{app} is the applied temperature gradient (from a furnace or another source). Both G_L^{app} and the ambient temperature of the gas phase T_∞ away from the MG interface are experimentally controllable parameters.

3. Equations of evolution

Let $\epsilon \equiv h_0/L_0 \ll 1$, where h_0 and L_0 are the characteristic film thickness and length, respectively, and rescale variables in the following manner appropriate for a thin film: $z = Zh_o$, $x = XL_o$, $t = \tau L_0/U_0$, $\overline{h}_C = \overline{H}_C h_0$, $\overline{h} = \overline{H}h_0$, $h = Hh_0$, $u = UU_0$, $w = W\epsilon U_0$, $p^* = P\mu U_0/(\epsilon^2 L_0)$ and $\phi = \Phi\mu U_0/(\epsilon^2 L_0)$. Here, $U_0 = \nu/L_0$ is chosen as a characteristic flow velocity for a fluid with kinematic viscosity ν. The temperature in the bulk melt is non-dimensionalized by $T^l = \Theta^l\Delta + T_M$ and bulk crystal by $T^s = \Theta^s\Delta + T_M$, where Δ is a reference temperature or temperature difference. The dimensionless capillary number, dimensionless latent heat parameter, and dimensionless Marangoni number are defined as $\overline{C}^{-1} \equiv \epsilon^3\gamma_0^{MG}/(\mu U_0)$, $\hat{\overline{L}} \equiv \epsilon L_v h_0 U_0/(k^l\Delta)$ and $\overline{M}_T \equiv \epsilon^{-2}\gamma_T^{CM}\Delta/\gamma_0^{MG}$, respectively. A list of symbols, and their values for pure aluminium, is given in table 1.

All dependent variables except for the interface shapes are expressed as regular perturbation series in terms of the small parameter ϵ^2, and are substituted into the governing equations. At leading order, the following system applies in the bulk melt:

$$P^*_X = U_{ZZ}, \tag{3.1}$$

$$P^*_Z = 0, \tag{3.2}$$

$$\Theta^l_{ZZ} = 0, \tag{3.3}$$

and

$$U_X + W_Z = 0. \tag{3.4}$$

Symbol	Description	Definition	Value
ϵ	thin film scaling parameter	$\frac{h_0}{L_0}$	0.001
$\hat{\hat{L}}$	latent heat of fusion	$\frac{\epsilon L_v h_0 U_0}{\Delta k^l}$	5.69×10^{-9}
β_T	ratio of conductivities	$\frac{k^s}{k^l}$	2.2
G_S	temperature gradient in solid	$\frac{G_L^{app} h_0}{\Delta}$	free parameter
Bi	Biot number	$\frac{\alpha_{Th} h_0}{k^l}$	5.3×10^{-7}
Θ_∞	far-field temperature in gas	$\frac{T_\infty - T_M}{\Delta}$	varies
m_L	liquidus slope	$\frac{m C_0}{\Delta}$	-5.6×10^{-4}
E	ratio of densities	$\frac{\rho^s}{\rho^l}$	1.07
$\overline{C}^{-1}$	capillary number	$\epsilon^3 \frac{\gamma_0^{MG}}{\mu U_0}$	1.68×10^{-5}
$\overline{\Gamma}$	crystal–melt surface parameter	$\epsilon^2 \frac{\gamma^{CM} T_M}{L_v h_0 \Delta}$	9.21×10^{-9}
$\overline{M}_T$	Marangoni due to temperature gradient	$\epsilon \frac{\overline{C}^{-1} \gamma_T^{MG} \Delta}{\gamma_0^{MG}}$	1.55×10^{-4}
$\tilde{A}$	dimensionless Hamaker constant	$\frac{A'}{6\pi h_0 \rho^l \nu^2}$	8.8×10^{-6}
Re	Reynolds number	$\frac{U_0 L_0}{\nu}$	1

TABLE 1. List of non-dimensional variables with values for pure aluminium.

At the MG interface ($Z = H$),

$$-P^* + P_G + \Phi = \overline{C}^{-1} H_{XX}, \tag{3.5}$$

where

$$\Phi = \frac{\tilde{A}}{(H - \overline{H})^3}, \tag{3.6}$$

and $\tilde{A} = A'/(6\pi h_0 \rho^l \nu^2)$ is a non-dimensional Hamaker constant. Furthermore,

$$U_Z = -\epsilon M_T C^{-1} \left(\Theta_X^l + H_X \Theta_Z^l \right), \tag{3.7}$$

$$W = H_\tau + U H_X, \tag{3.8}$$

and

$$\Theta_Z^l = -Bi(\Theta^l - \Theta_\infty). \tag{3.9}$$

$\Theta_\infty = (T_\infty - T_m)/\Delta$ is the scaled ambient gas temperature and $Bi = \alpha_{Th} h_0 / k^l$ is the Biot number for heat transfer through the MG interface.

At the CM interface ($Z = \overline{H}$) the non-dimensional boundary conditions are

$$\Theta_I = \epsilon^2 \Gamma \overline{H}_{XX}, \tag{3.10}$$

$$W = (1 - E)\overline{H}_\tau + U \overline{H}_X, \tag{3.11}$$

and

$$U = 0. \tag{3.12}$$

The dimensionless CM surface tension is $\Gamma=\gamma^{CM}T_M/(L_v h_0\Delta)$ and $E=\rho^s/\rho^l$ is the ratio of the crystal to melt densities.

It is noted that the CM surface tension could be retained at this order also. However, from estimates of the magnitude of this effect, it is anticipated that the influence of the CM surface tension would not be important in the parameter ranges of interest in this study, i.e. for disturbances near the maximum growth rate as given by a linear stability analysis. For this reason, we neglect the effect of the CM surface tension.

The balance of heat at the crystal–melt interface requires knowledge of the temperature in the crystal. Suppose we assume the crystal layer to be very thin (having a thickness $\overline{h}_c\sim h_o$); then the temperature is governed by $\Theta^s_{ZZ}=0$, which, when combined with the component of the applied temperature gradient at the lower crystal surface, gives a field linear in Z. It follows then that the final CM interfacial condition becomes

$$\hat{\hat{L}}\overline{H}_\tau=\beta_T G_S-\Theta^l_Z, \tag{3.13}$$

where β_T is the ratio of the crystal to melt thermal conductivity and $G_S=G_L^{app}(h_0/\Delta)$ is the dimensionless applied temperature gradient in the crystal. The effect of the thermal field in the crystal is only through the parameter G_S. Finally, initial conditions and lateral boundary conditions for all variables are prescribed. Δ is also chosen to be the bulk melting temperature T_M.

Evolution equations for $H_\tau(\tau,X)$ and $\overline{H}_\tau(\tau,X)$ are derived as follows. According to (3.2), the pressure is independent of Z, therefore (3.1) is integrated and, with the conditions (3.7) and (3.12), gives

$$U(\tau,X,Z)=\frac{1}{2}P^*_X(Z^2-\overline{H}^2)-\left[P^*_XH+\overline{C}^{-1}\overline{M}_T\left(\Theta^l_X+H_X\Theta^l_Z\right)\right](Z-\overline{H}). \tag{3.14}$$

Integration of (3.4) gives $W(\tau,X,Z)$. Equation (3.3) is also integrated and, after applying the boundary conditions (3.9) and (3.10), gives

$$\Theta^l=\frac{Bi(\Theta_\infty)}{1+Bi(H-\overline{H})}(Z-\overline{H}). \tag{3.15}$$

Evolution equations for $H_\tau(\tau,X)$ and $\overline{H}_\tau(\tau,X)$ follow by combining (3.5), the kinematic equations (3.8) and (3.11), and the heat conservation law (3.13) with (3.14). The result is

$$\overline{H}_\tau=\frac{1}{\hat{\hat{L}}}\left(\beta_T G_S-\frac{Bi\Theta_\infty}{1+Bi(H-\overline{H})}\right) \tag{3.16}$$

and

$$H_\tau-(1-E)\overline{H}_\tau=\left[-\frac{\tilde{A}(H-\overline{H})_X}{(H-\overline{H})}-\frac{\overline{C}^{-1}}{3}(H-\overline{H})^3H_{3X}\right.$$
$$\left.+\overline{C}^{-1}\left[\frac{\overline{M}_T Bi\Theta_\infty[H-\overline{H}]}{2(1+Bi[H-\overline{H}])}\right]_X(H-\overline{H})^2\right]_X. \tag{3.17}$$

In order to allow for comparison with previous analysis, such as the case of an isothermal film on a substrate, spatial and temporal coordinates are rescaled in terms of the capillary and Hamaker parameters according to $\hat{X}=\sqrt{(3\tilde{A}/\overline{C}^{-1})}X$ and

$\hat{\tau} = (3\tilde{A}^2/\overline{C}^{-1})\tau$, to give

$$\overline{H}_{\hat{\tau}} = Q - \frac{RBi}{1 + Bi(H - \overline{H})} \tag{3.18}$$

$$H_{\hat{\tau}} - (1 - E)\overline{H}_{\hat{\tau}} = \left[\left(M \frac{Bi(H - \overline{H})^2}{1 + Bi[H - \overline{H}]^2} - \frac{1}{[H - \overline{H}]} \right) [H - \overline{H}]_{\hat{X}} - (H - \overline{H})^3 H_{3\hat{X}} \right]_{\hat{X}} . \tag{3.19}$$

A new solidification parameter,

$$R = \frac{\overline{C}^{-1} \Theta_\infty}{3\tilde{A}^2} \frac{1}{\hat{\hat{L}}}, \tag{3.20}$$

the modified Marangoni number,

$$M = \frac{\overline{C}^{-1} \overline{M}_T \Theta_\infty}{2\tilde{A}}, \tag{3.21}$$

and the heat flux through the crystal,

$$Q = \frac{\beta_T G_S \overline{C}^{-1}}{3\tilde{A}^2 \hat{\hat{L}}}, \tag{3.22}$$

are identified. The parameters appearing in (3.18) and (3.19) are R, Q, Bi, E and M. The nonlinear system of evolution equations (3.18) and (3.19) govern long-wave interface dynamics subject to an applied body force potential, capillary, thermocapillary, heat flow and solidification effects.

Note that for $\Theta_\infty = 0$ then $R = M = 0$. Furthermore, if $E = 1$ and $\overline{H} = 0$ then this isothermal system reduces to the case of a thin film on a substrate studied by Williams & Davis (1982), which serves as a benchmark, from which it is possible to ascertain the importance of the thermal/solidification effects.

4. Linear stability analysis

Linear stability of the system of equations (3.18) and (3.19) is studied by considering perturbations of the interface shape functions H and $\overline{H}$ from a uniformly thin base state:

$$\left. \begin{aligned} H(\hat{\tau}, \hat{X}) &= H(\hat{\tau})^0 + H(\hat{\tau}, \hat{X})^1, \\ \overline{H}(\hat{\tau}, \hat{X}) &= \overline{H}(\hat{\tau})^0 + \overline{H}(\hat{\tau}, \hat{X})^1, \end{aligned} \right\} \tag{4.1}$$

where superscripts 0 and 1 refer to the base and the perturbed states, respectively. These functions are substituted into (3.18) and (3.19) to give

$$\overline{H}^0_{\hat{\tau}} = Q - \frac{RBi}{(1 + Bi(H^0 - \overline{H}^0))} \tag{4.2}$$

and

$$H^0_{\hat{\tau}} - (1 - E)\overline{H}^0_{\hat{\tau}} = 0. \tag{4.3}$$

governing the base state. A time-independent base state is investigated (i.e. $\overline{H}^0_{\hat{\tau}}=0$, $H^0_{\hat{\tau}}=0$, $\overline{H}^0=0$ and $H^0=1$). Since $\Theta_\infty \geqslant 0$ then the heat flux through the melt layer,

$$Q=\frac{RBi}{(1+Bi)}, \tag{4.4}$$

is fixed by (4.2).

The linearized perturbation equations are given by

$$\overline{H}^1_{\hat{\tau}}=\frac{RBi^2}{(1+Bi)^2}(H^1-\overline{H}^1) \tag{4.5}$$

and

$$H^1_{\hat{\tau}}-(1-E)\overline{H}^1_{\hat{\tau}}=\left(M\frac{Bi[H^0-\overline{H}^0]^2}{(1+Bi[H^0-\overline{H}^0]^2)}-\frac{1}{[H^0-\overline{H}^0]}\right)(H^1-\overline{H}^1)_{2\hat{X}} \\ -[H^0-\overline{H}^0]^3H^1_{4\hat{X}}. \tag{4.6}$$

Substituting normal modes for the perturbation shapes,

$$H^1=\rho\exp(\sigma\hat{\tau})\exp(\mathrm{i}\omega\hat{X}) \tag{4.7}$$

and

$$\overline{H}^1=\overline{\rho}\exp(\sigma\hat{\tau})\exp(\mathrm{i}\omega(\hat{X}-\hat{X}_0)), \tag{4.8}$$

where σ is the growth rate, ω is a wavenumber and $\hat{X}_0$ allows for a translation of the CM interface relative to the MG interface, leads to the dispersion relation

$$\sigma^2+\left[\omega^4+\frac{MBi-(1+Bi)^2}{(1+Bi)^2}\omega^2+\frac{Bi^2RE}{(1+Bi)^2}\right]\sigma+\frac{RBi^2}{(1+Bi)^2}\omega^4=0. \tag{4.9}$$

The marginal stability condition, obtained by setting the real component of σ equal to zero in the dispersion relationship, is given by the heavy black curve in figure 2(*a*) on a diagram of the thermal parameter $B=\overline{C}^{-1}Bi^2\Theta_\infty/(3\hat{\tilde{L}}\tilde{A}^2(1+Bi)^2)$ versus ω. The values of all coefficients in (4.9) are calculated from the data for Al given in table 2. Within the marginal curve the film is unstable, outside the curve it is stable. The isothermal flat-CM interface occurs at $B=0$ and exhibits a range of unstable wavenumbers. As B increases from 0, the range of unstable perturbation wavenumbers shrinks culminating in a maximum value of $B_C=0.234$ along the marginal stability surface.

The solid to liquid density ratio E allows for volume shrinkage ($E>1$) or expansion ($E<1$) as a system solidifies. Figure 2(*b*) shows the influence of variation in E on the marginal stability condition. The value of E for Al is 1.07. Values of E below unity correspond to systems such as water/ice. Notice that the region of instability, below the heavy curve, expands as the density ratio decreases, hence the system becomes less stable. For E greater than unity, hotter fluid flows to the tips of the perturbations on the CM interface and fluid is rejected at the depressions. For E less than unity, the fluid is rejected at tips and additional hot fluid flows to the depressions. These effects are consistent with the results shown in figure 2(*b*).

From this point on, it is assumed that $E=1$ and $M=0$, since Marangoni effects and the density differences modify the results but are not the primary focus of the study. The dispersion relation now depends on the single control parameter B. It also

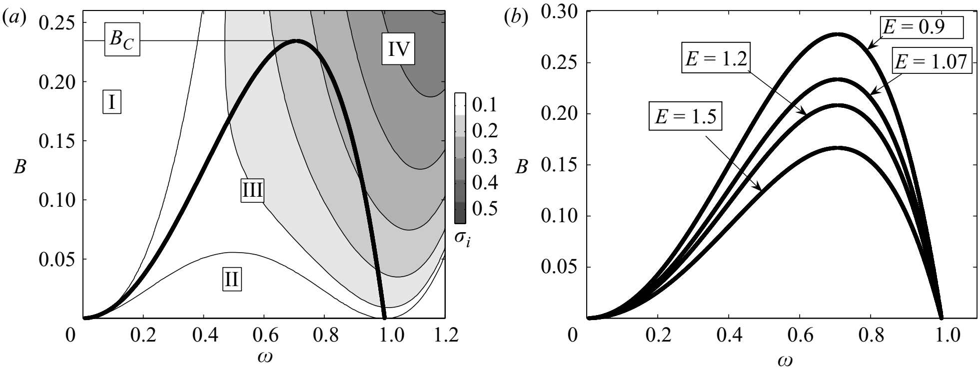

FIGURE 2. (*a*) Stability plot as a function of the thermal parameter B. The heavy black curve is the marginal stability limit. Perturbation conditions below this curve are unstable, and conditions above are stable. Onset of instability occurs at a critical thermal parameter $B_C = 0.234$. The white regions represent stationary initial conditions, while the grey-scale contours represent iso-frequency oscillatory states. Region I is therefore stationary and stable. Region II is stationary but unstable, region III is oscillatory and unstable, and region IV is oscillatory and stable. (*b*) Marginal stability limits for a few values of E, the ratio of solid to liquid densities, plotted as a function of B.

Symbol	Description	Al	Units
h_0	film thickness	10^{-8}	m
L_0	film length	10^{-5}	m
L_v	latent heat of fusion	1.01×10^9	J m^{-3}
U_0	characteristic fluid velocity (ν/L_0)	0.05	m s^{-1}
Δ	set equal to T_m	934	K
T_m	melting temperature	934	K
T_∞	far-field temperature in gas	varies	K
k^l	thermal conductivity of liquid	95	W m^{-1} K^{-1}
k^s	thermal conductivity of solid	210	W m^{-1} K^{-1}
c^l	specific heat capacity of liquid	2.58×10^6	J m^{-3} K^{-1}
G_L^{app}	applied temperature gradient in solid	varies	K m^{-1}
α_{Th}	convective heat transfer coefficient	$10 - 10^4$	W m^{-2} K^{-1}
ρ^s	density of solid	2.55×10^3	Kg m^{-3}
ρ^l	density of liquid	2.39×10^3	Kg m^{-3}
γ_0^{MG}	MG surface tension (at 954 K)*	1.007	N m^{-1}
γ^{CM}	CM surface tension	0.093	N m^{-1}
μ	viscosity ($\nu\rho^l$)†	1.2×10^{-3}	N s m^{-2}
ν	kinematic viscosity	5.02×10^{-7}	m^2 s^{-1}
A'	Hamaker constant	$10^{-19} - 10^{-21}$	J

* From Anson, Drew & Gruzleski (1999) and Hur, Park & Hiroshi (1989).† From Dinsdale and Quested (1999).

TABLE 2. List of dimensional parameters for pure aluminium.

follows that, for $\sigma = \sigma_r + \mathrm{i}\sigma_i$, then from (4.9)

$$\left.\begin{aligned} \sigma_r^2 - \sigma_i^2 + \sigma_r(B - \omega^2 + \omega^4) + B\omega^4 &= 0, \\ \sigma_i[2\sigma_r + (B - \omega^2 + \omega^4)] &= 0. \end{aligned}\right\} \tag{4.10}$$

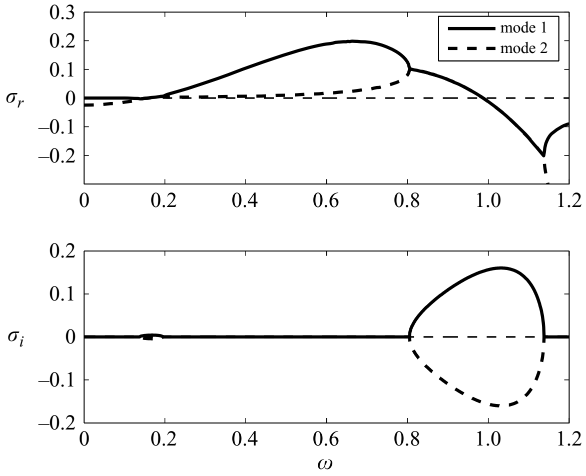

FIGURE 3. Real and imaginary parts of the growth rate σ for a value of the thermal parameter $B = 0.0246$. A perturbation of maximum growth rate is stationary, although perturbations having marginally stable wavenumbers are oscillatory.

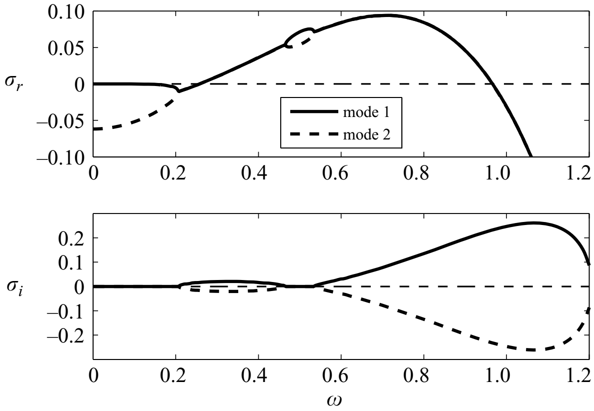

FIGURE 4. Real and imaginary parts of the growth rate σ for a value of the thermal parameter $B = 0.062$. Here a perturbation of maximum growth rate is unstable to oscillatory modes, as are perturbations having marginally stable wavenumbers.

In the fully nonlinear system the phase shift X_o has a significant effect on the evolving interfaces. Again, for the isothermal case $B = 0$, there is one non-vanishing mode, identical to that obtained by Williams & Davis (1982), i.e. $\sigma = \omega^2(1 - \omega^2)$.

Two representative examples of the dispersion relation are plotted in figure 3 and figure 4 for the cases of $B = 0.0246$ and $B = 0.062$, respectively. Perturbations having wavenumber of maximum growth rate are stationary in the case $B = 0.0246$ as σ is real. However, marginally stable perturbations are oscillatory. In the second case, the perturbation having maximum growth rate is also oscillatory.

The ratio of the linear perturbation amplitudes of the crystal–melt and melt–gas surfaces $[\rho, \overline{\rho}]$ is fixed by the solution of the appropriate generalized eigenvalue problem resulting from the linearization of the evolution equations. The ratio of the

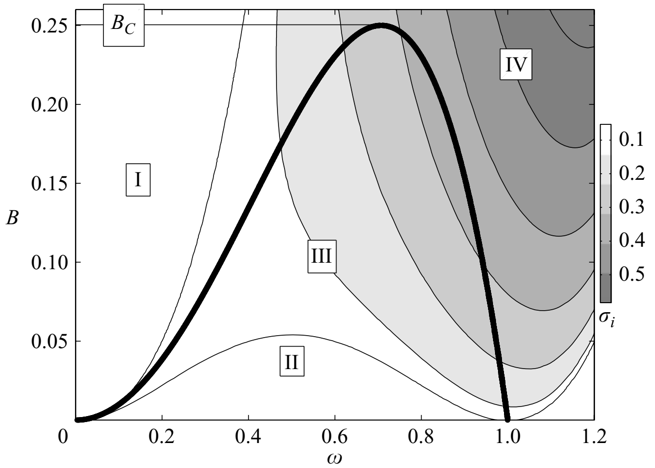

FIGURE 5. Stability plot as a function of the thermal parameter B for $E = 1$ and $M = 0$. The heavy black curve is the stability limit. The white regions represent non-oscillatory states, while the grey-scale contours represent iso-frequency oscillatory states as in figure 2.

amplitudes is

$$\frac{\overline{\rho}}{\rho} = \frac{B}{(\sigma + B)} \exp(\mathrm{i}\omega\hat{X}_0). \tag{4.11}$$

Utilizing (4.11) in the expressions for the linearized shape growth rates gives:

$$\left.\begin{aligned} \frac{\mathrm{d}H^1}{\mathrm{d}\hat{\tau}} &= \left[\frac{\omega^2}{\left(1 + \dfrac{B}{\sigma}\right)} - \omega^4\right] H^1, \\ \frac{\mathrm{d}\overline{H}^1}{\mathrm{d}\hat{\tau}} &= \sigma\overline{H}^1. \end{aligned}\right\} \tag{4.12}$$

The marginal stability diagram for the case of $E = 1$, $M = 0$ is given in figure 5, which is similar to figure 2, except that the marginal stability surface has shifted up slightly, and the maximum increases from $B = 0.234$ to $B = 0.250$.

Oscillatory behaviour occurs when the discriminant of the solution of the dispersion relation in (4.9) becomes negative. The critical values of the thermal parameter $B(\omega)$ separating regions of stationary and oscillatory instabilities are $B_C^{\pm} = \omega^2 + \omega^4 \pm 2\omega^3$. These critical lines are shown in figure 5 as the lines separating the white from the shaded regions in the plot. Only the root B_C^- within the unstable region is relevant since these oscillatory solutions grow. For the case in which $B < B_C^- = \omega^2 + \omega^4 - 2\omega^3$, then there are no oscillatory solutions ($\sigma_i = 0$) and thus

$$\sigma_r = -\tfrac{1}{2}(B - \omega^2 + \omega^4) \pm \tfrac{1}{2}\{(B - \omega^2 + \omega^4)^2 - 4B\omega^4\}^{1/2}. \tag{4.13}$$

If $B > B_C^-$ then

$$\left.\begin{aligned} \sigma_r &= -\tfrac{1}{2}(B - \omega^2 + \omega^4), \\ \sigma_i &= \pm\left[-\tfrac{1}{4}(B - \omega^2 + \omega^4)^2 + B\omega^4\right]^{1/2}. \end{aligned}\right\} \tag{4.14}$$

Of particular interest is the observation that, in the case that B is finite and for $\sigma_r = 0$, σ_i only vanishes if ω vanishes. All non-isothermal marginally stable states ($\sigma_r = 0$) are oscillatory: thus, one expects either travelling or standing wave disturbances. In the case $\sigma_r = 0$, then $\sigma_i = \sqrt{B}w^2$, meaning that the oscillation frequency is larger for larger B on the marginal curve. The maximum of the marginal stability curve occurs where $\sigma_r = \mathrm{d}\sigma_r/\mathrm{d}\omega = 0$, at which point $B = 0.25$ and $\omega = \sqrt{2}/2$. Thus increasing B *stabilizes* the film, as the effect of the thermal field overrides the destabilizing effect of the van der Waals interactions.

5. Physical mechanisms

Comparing to the isothermal case, the capillary and the van der Waals forces couple with the solidification effects to produce oscillatory instability. The fact that the crystal–melt interface is deformable impacts the relative importance of the thermal, capillary and van der Waals effects.

The linearized growth rates of the interface shapes can be given in terms of the eigenfunctions in $(\hat{X}, \hat{\tau})$ variables:

$$\left.\begin{aligned} \frac{\mathrm{d}H^{(1)}}{\mathrm{d}\hat{\tau}} &= W^{(1)}, \\ \frac{\mathrm{d}\overline{H}^{(1)}}{\mathrm{d}\hat{\tau}} &= -\frac{1}{\hat{\hat{L}}}\Theta_Z^{l(1)}, \end{aligned}\right\} \tag{5.1}$$

where the function $W^{(1)}$ is evaluated at the unperturbed MG interface and $\Theta_Z^{l(1)}$ is evaluated at the unperturbed CM interface. So, the upper interface perturbation growth rate depends explicitly on the vertical component of the fluid velocity (through the kinematic condition) and the CM interface growth rate is proportional to the derivative of the temperature with respect to Z in the melt at the interface. However, both eigenfunctions depend on both of the perturbed interface shapes unless the system is isothermal, illustrating that growth rates are coupled through the thermal field. The eigenfunctions are written as

$$\begin{aligned} U^{(1)}\{\hat{X}, Z, \hat{\tau}\} = {} & \mathrm{i}\omega\big[-3\tilde{A}\big(H^{(1)}\{\hat{X}, \hat{\tau}\} - \overline{H}^{(1)}\{\hat{X}, \hat{\tau}\}\big) \\ & -\overline{C}^{-1}(\mathrm{i}\omega)^2 H^{(1)}\{\hat{X}, \hat{\tau}\}\big]\left(\frac{Z^2}{2} - Z\right), \end{aligned} \tag{5.2}$$

$$\begin{aligned} W^{(1)}\{\hat{X}, Z, \hat{\tau}\} = {} & \omega^2\big[-3\tilde{A}\big(H^{(1)}\{\hat{X}, \hat{\tau}\} - \overline{H}^{(1)}\{\hat{X}, \hat{\tau}\}\big) \\ & +\overline{C}^{-1}\omega^2 H^{(1)}\{\hat{X}, \hat{\tau}\}\big]\left(\frac{Z^3}{6} - \frac{Z^2}{2}\right), \end{aligned} \tag{5.3}$$

$$\begin{aligned} \Theta^{l(1)}\{\hat{X}, Z, \hat{\tau}\} = {} & -\left[\frac{Bi^2\Theta_\infty}{(1+Bi)^2}\right]\big(H^{(1)}\{\hat{X}, \hat{\tau}\} - \overline{H}^{(1)}\{\hat{X}, \hat{\tau}\}\big)Z \\ & -\left[\frac{Bi\,\Theta_\infty}{(1+Bi)}\right]\overline{H}^{(1)}\{\hat{X}, \hat{\tau}\}, \end{aligned} \tag{5.4}$$

and

$$P^{(1)}\{\hat{X}, \hat{\tau}\} = -3\tilde{A}\big(H^{(1)}\{\hat{X}, \hat{\tau}\} - \overline{H}^{(1)}\{\hat{X}, \hat{\tau}\}\big) + \overline{C}^{-1}\omega^2 H^{(1)}\{\hat{X}, \hat{\tau}\}. \tag{5.5}$$

The eigenfunctions (5.2)–(5.5) can be used to reveal the effects of the thermal field and the basic mechanisms for instability and stabilization of the layer.

Consider a perturbation of fixed, unstable wavenumber in an isothermal system. Instability arises for those ranges of wavelengths in which the destabilizing van der Waals forces (proportional to the square of the wavenumber) are stronger than the stabilizing capillary forces (proportional to the fourth power of the wavenumber).

Along the perturbed interface, the van der Waals forces will be stronger at the narrowest regions of the film, and the capillary forces will be strongest at regions of high curvature. Now let the far-field temperature be increased, thereby introducing a *positive* temperature gradient in the direction pointing from crystal to the gas phase in the transverse direction of the film. For small enough gradients, below B_C^- in region II in figure 5, the instability is stationary. Because the film is thin, and the Prandtl number is vanishingly small, heat flow is quasi-static. Therefore heat enters at the MG interface and is immediately transported to the CM interface, at which point it may be absorbed by the crystal as latent heat. At the narrowest region there will be more heat transferred than at the wider regions, providing more of a tendency of the CM interface to decrease its growth rate or even melt locally. This then is a thermal mechanism of film stabilization which directly opposes the destabilizing influence of the van der Waals forces. (This picture is validated in the next section in figure 18.)

If the far-field temperature is increased yet further at fixed, unstable wavenumber so that $B > B_C^-$ but $\sigma_r > 0$, then the amount of heat arriving at the CM interface is increased to such a degree that at the narrowest region of the perturbed film the CM interface will now ‘outrun’ the MG interface, resulting in an expansion of the initially narrowest region. The increase in separation reduces the magnitude of the van der Waals forces locally at this region. Meanwhile, due to fluid conservation and an increase in capillary forces in the descending portion of the MG interface regions, the adjacent initially wider regions of the thin layer begin to narrow, bringing the van der Waals forces increasingly into play, which continues to draw the interfaces closer in the now narrowing regions. However, once again, as the regions become thinner, the fast transport of heat to the narrowing region of the CM interface causes deceleration of the thinning of this portion of the film since there is sufficient latent heat to promote melting. Thus, for $B > B_c^-$ in the oscillatory unstable region of the marginal stability area, the temperature gradient is large enough that the melting process can locally ‘outrun’ the MG interface, which is descending due to van der Waals forces at the narrowest regions, but only for a limited time. The cycle then reverses itself so that the region of the interface which was just previously narrowing expands, and the region which was previously expanding begins to narrow. The numerical calculations show that, after a number of cycles, the van der Waals forces win out, resulting in rupture. If the configuration of the MG and CM interfaces has symmetry then, the result is the growth of a standing wave; if not symmetric, then it is the growth of a travelling wave. Finally, if the ambient gas temperature is large enough, then the van der Waals forces cannot overcome the large amount of heat that is being transported to the CM interface, and the thin film is rendered stable.

In the oscillatory range, the relationship between the perturbed surface shapes is complicated and, in general, the shapes are out of phase. Figure 6 is a plot of the eigenfunctions for one of the pair of unstable complex conjugate eigenvalues, which shows that, for both the CM and MG interface, the interface velocity is out of phase with the perturbed surface shape for $B = 0.062$ and $\omega = 0.707$.

Plots of one of the eigenfunctions for the temperature, pressure and vertical fluid velocity component fields, evaluated at the MG interface, are given in figure 7, for the cases in which $B < B_C^-$ ($\sigma_i = 0$) and $B > B_C^-$ ($\sigma_i > 0$). The figure illustrates the phase difference that arises between the shape and the eigenfunctions as σ becomes complex and gives rise to oscillatory behaviour. The imaginary part of σ_i produces a phase shift between the CM and the MG interface and between shape and temperature eigenfunctions as shown in the figures, leading to a travelling disturbance. Numerical

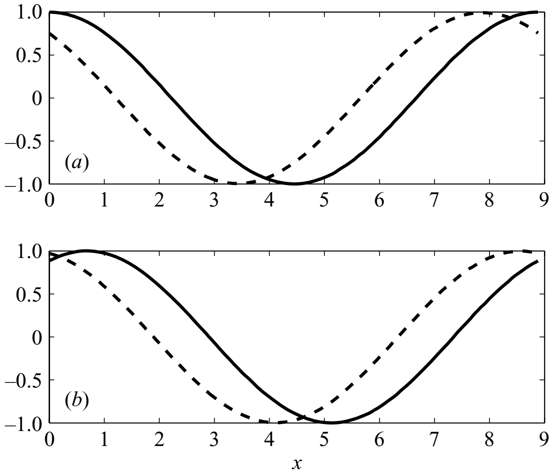

FIGURE 6. Surface shape (solid) and velocity (dashed) eigenfunctions for $B > B_C^-$ in the oscillatory regime. Subplot (*a*) is for the μG interface and (*b*) is for the CM interface. All eigenfunctions are normalized by the maximum values.

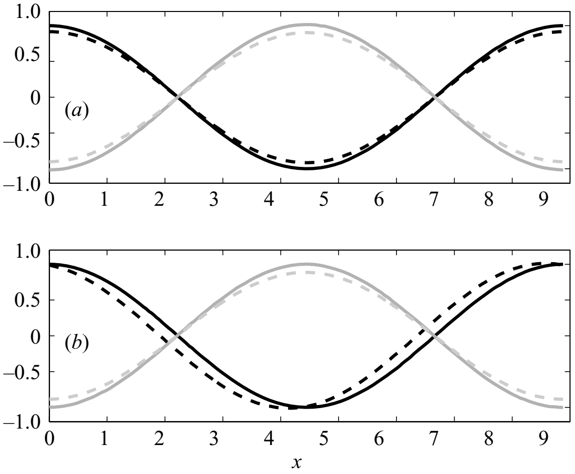

FIGURE 7. Surface shape (solid black), interface temperature (dashed black), vertical flow (solid grey) and pressure (dashed grey) normalized eigenfunctions at the MG interface. (*a*) is for $B < B_C^-$ in the stationary regime and (*b*) is for $B > B_C^-$ in the oscillatory regime.

analysis in the next section will shed further light on the coupling beyond the initial instability.

6. Numerical method

In this section, the governing pair of equations are discretized and numerically integrated to find the evolution of the interface shapes and to predict rupture times. Equation (3.19) of the nonlinear system (3.18) and (3.19) is rewritten in the form

$$H_{\hat{\tau}} = (f(H, \overline{H})(H - \overline{H})_{\hat{X}} + g(H, \overline{H})H_{3\hat{X}})_{\hat{X}}, \tag{6.1}$$

where

$$f(H, \overline{H}) = -\frac{1}{H - \overline{H}}$$

and

$$g(H, \overline{H}) = -(H - \overline{H})^3.$$

The right-hand side of (6.1) is then discretized using a modified conservative finite difference scheme on a uniform grid (A. A. Golovin & D. L. Chopp, personal communication 2005)

$$\begin{aligned} &- \left(f_{i+1/2}\left(H^n_{i+1} - H^n_i\right) - f_{i-1/2}\left(H^n_i - H^n_{i-1}\right)\right)\frac{1}{\Delta x^2} \\ &+ \left(f_{i+1/2}\left(\overline{H}^n_{i+1} - \overline{H}^n_i\right) - f_{i-1/2}\left(\overline{H}^n_i - \overline{H}^n_{i-1}\right)\right)\frac{1}{\Delta x^2} \\ &- \left(g_{i+1/2}\left(H^n_{i+2} - 3H^n_{i+1} + 3H^n_i - H^n_{i-1}\right)\right)\frac{1}{\Delta x^4} \\ &+ \left(g_{i-1/2}\left(H^n_{i+1} - 3H^n_i + 3H^n_{i-1} - H^n_{i-2}\right)\right)\frac{1}{\Delta x^4}, \end{aligned} \tag{6.2}$$

where

$$f_{i\pm1/2} = \frac{f_i + f_{i\pm1}}{2} \tag{6.3}$$

and

$$g_{i\pm1/2} = \frac{g_i + g_{i\pm1}}{2}. \tag{6.4}$$

Periodic boundary conditions are applied at the left and right endpoints of the spatial grid. The equations are updated in time using a backward difference scheme with a quasi-constant step size that is provided by the MATLAB function *ODE15S* (Shampine & Reichelt 1997). The scheme is stable and conserves mass for all initial conditions and mesh sizes considered.

The numerical results for the evolution to rupture of a MG interface and a flat CM interface, under isothermal conditions, can be compared to previous research. Under isothermal conditions, only destabilizing attractive van der Waals forces compete with the stabilizing capillary effects. The evolution of the MG interface will result in film rupture if the initial perturbation is selected to correspond to an unstable wavenumber from linear stability theory, i.e. $0 < \omega < 1$. Figure 8 shows the MG interface morphology as the initial perturbation grows and approaches rupture. The wavenumber that corresponds to the maximum real growth rate was selected and the initial perturbation amplitude is 0.1.

Time to rupture $\hat{\tau}_R$ is plotted as a function of the number of spatial nodes in figure 9. Our results show that $\hat{\tau}_R$ converges to 4.08, a value that compares reasonably well with previous results. (Burelbach *et al.* 1988) used central finite differences in space and the midpoint (Crank–Nicholson) rule in time, and solved the difference equations using Newton–Raphson iteration. They report a rupture time of $\hat{\tau}_R = 4.16$ with $N = 40$ spatial nodes. Williams & Davis (1982) employed a finite difference midpoint method and report $\hat{\tau}_R = 5.7$ with $N = 16$.

As the film nears rupture, the curvature of the tip becomes very large. Figure 10 is a plot of the position H and inverse curvature $1/\mathscr{K} = 1/H_{\hat{X}\hat{X}}$ of the tip, along with the grid spacing Δx (horizontal dashed line) for reference. As the inverse curvature diminishes to the same order of magnitude as the uniform grid spacing Δx, the grid is no longer fine enough to resolve the tip. Thus, numerical accuracy suffers at times

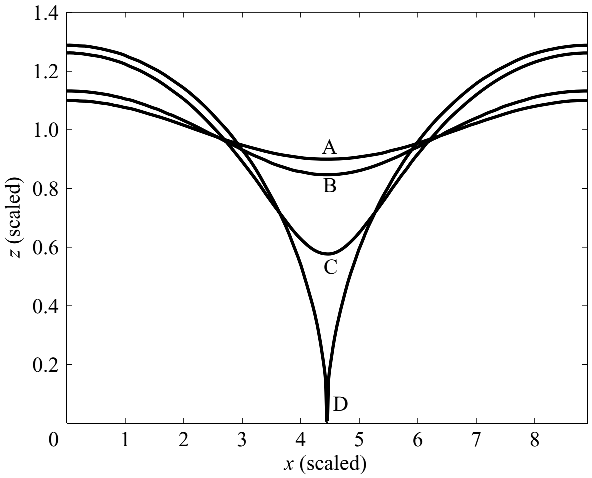

FIGURE 8. Isothermal rupture of film with flat CM interface for a sequence of times. Curve A is the initial perturbation with amplitude 0.1 at $\hat{\tau}=0$. Curve B is at $\hat{\tau}=1.45$, C is at $\hat{\tau}=3.77$ and D is at rupture $\hat{\tau}_R=4.08$. 800 spatial nodes were used to discretize the interface.

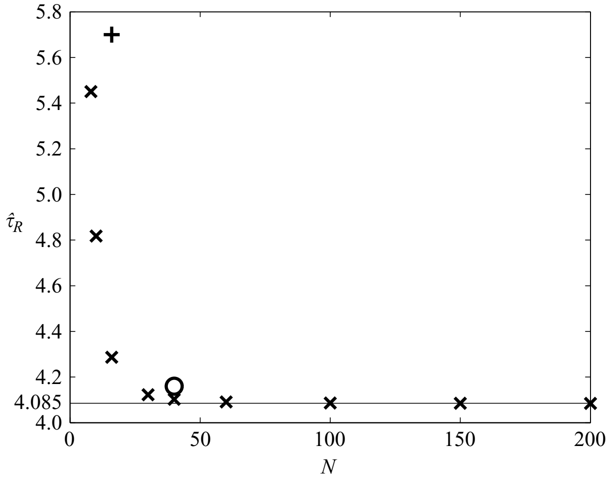

FIGURE 9. Comparison of rupture time $\hat{\tau}_R$ as a function of number of spatial nodes for the same initial perturbation amplitude. $\hat{\tau}_R$ has converged to 4.08 by approximately $N=100$. The '+' and '○' symbols give the rupture times predicted in Williams & Davis (1982) and Burelbach *et al.* (1988), respectively.

greater than $\hat{\tau}_L$, where $\hat{\tau}_R-\hat{\tau}_L=4\times10^{-5}$ for $N=400$ nodes. This is a very small fraction of $\hat{\tau}_R$, and resolution improves on finer grids. On the other hand, the work of Zhang & Lister (1999) shows how, for solutions to a class of thin film differential equations (that includes our isothermal case), an initial sinusoidal perturbation evolves into a similarity solution. Their conclusion is that the lubrication approximation is valid up to within a molecular length of separation between interfaces. Our calculations also show the rupture surface converging to similarity solutions, in both isothermal and non-isothermal cases. Therefore, our model is limited by numerical accuracy, not the breakdown of the lubrication approximation.

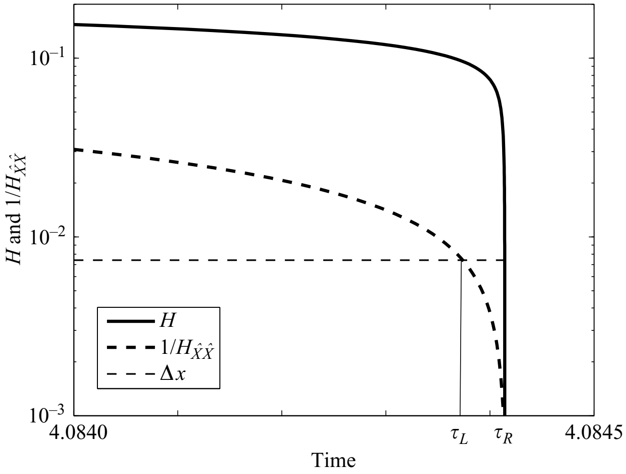

FIGURE 10. Position H and inverse curvature $1/H_{\hat{X}\hat{X}}$ of the tip as the film approaches rupture. The grid spacing Δx corresponds to the horizontal dashed line, and is no longer fine enough to resolve the tip when it is on the order of $1/H_{\hat{X}\hat{X}}$. Here this occurs at a time very close to rupture $\hat{\tau}_L = 4.0844$ ($\hat{\tau}_R = 4.08447$).

7. Nonlinear evolution with variable temperature

Numerical methods are applied to explore oscillatory and non-oscillatory evolution up to rupture. Both the MG and CM interfaces were discretized with 800 spatial nodes in the series of figures 11 to 14.

7.1. *Non-oscillatory interface evolution*

Numerical investigation of the fully nonlinear evolution shows how a phase shift in the initial condition has a significant effect on the long-term evolution of the system. The fully nonlinear system is evaluated for initial perturbations taken from region II within the marginal stability curve (figure 5), at $\Theta_\infty = 0.0156$ and wavenumber $\omega = 0.582$. Three different initial configurations of CM and MG interfaces are considered, corresponding to phase shifts of 0 (sinuous mode), π (pinch mode) and $\pi/2$ (symmetry-breaking mode). The amplitudes of the initial perturbations of the interfaces are chosen to be the eigenvectors given by the linear theory.

The greatest minimum separation between surfaces occurs when the initial perturbations are in phase. This initial condition requires the longest time to rupture, $\hat{\tau}_R = 23.5$. Evolution of the two surfaces at several times is shown in figure 11. The CM interface retreats from the approaching MG surface tip by melting back into the crystal region. As discussed in the previous section, there is sufficient latent heat being transferred quasi-statically to the CM surface near the rupture tip to drive local melting.

The initial surface configuration having the narrowest separation is the pinch mode, and time to rupture is shorter, $\hat{\tau}_R = 13.7$, than other configurations. Figure 12 again shows the crystal–melt interface retreating from the rupture tip region by melting.

The initial surfaces have an intermediate minimum separation for a phase shift of $\pi/2$, and an intermediate rupture time $\hat{\tau}_R = 16.5$. As in the pinch and sinuous modes, figure 13 shows the CM interface again retreating into the crystal away from the rupture tip.

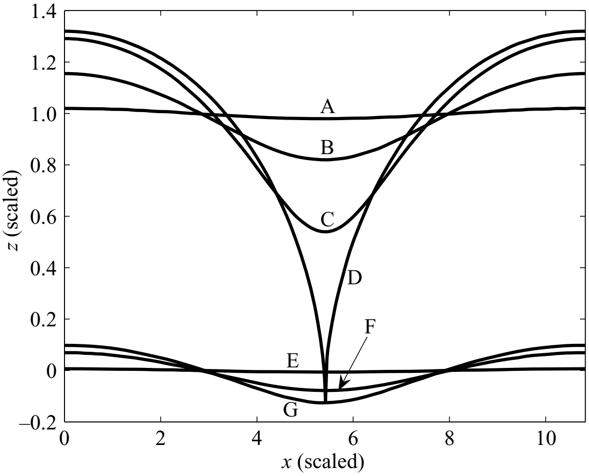

FIGURE 11. Evolution of sinuous or in-phase mode. According to linear theory, the initial perturbation condition of the two surfaces is in the stationary regime ($B = 0.054$, $\omega = 0.582$, $\sigma = 0.1154$). A rising temperature gradient in the region near the advancing tip drives melt-back of the crystal surface. The curves for the MG interface are labelled A–D, at times $\hat{\tau} = 0$, $\hat{\tau} = 17.9$, $\hat{\tau} = 22.8$ and $\hat{\tau} = 23.5$, respectively. Curves for the CM interface are labelled E–G, at times $\hat{\tau} = 0$, $\hat{\tau} = 20.7$ and $\hat{\tau} = 23.5$, respectively. The tip accelerates as it approaches the approximate rupture time of $\hat{\tau}_R = 23.5$.

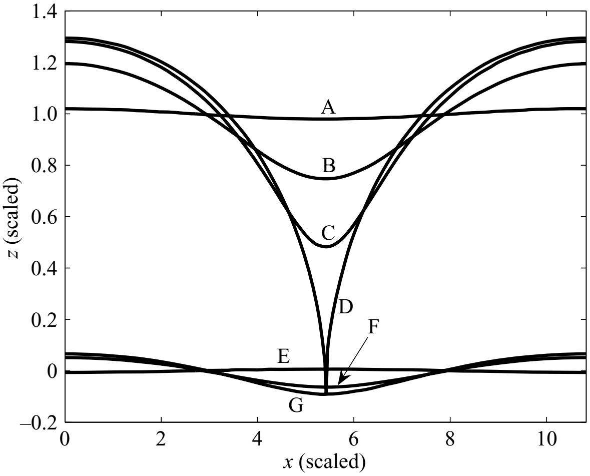

FIGURE 12. Evolution of pinch mode with the same initial conditions as figure 11, except that the CM interface is now π radians out of phase. According to linear theory, the initial perturbation condition of the two surfaces is in the stationary regime. The curves for the MG interface are labelled A–D, at times $\hat{\tau} = 0$, $\hat{\tau} = 11.2$, $\hat{\tau} = 13.4$ and $\hat{\tau} = 13.7$, respectively. Curves for the CM interface are labelled E–G, at times $\hat{\tau} = 0$, $\hat{\tau} = 12.5$ and $\hat{\tau} = 13.7$, respectively. The tip accelerates as it approaches rupture.

The temperature in the gas is maintained at a constant value. This results in a temperature profile in the melt layer that increases very slightly from T_M at the crystal–melt interface and jumps up to T_∞ just outside the melt–gas surface. Figure 14 is a contour plot of the scaled temperature field at a time near rupture. The rupture tip region has sliced through the isotherms.

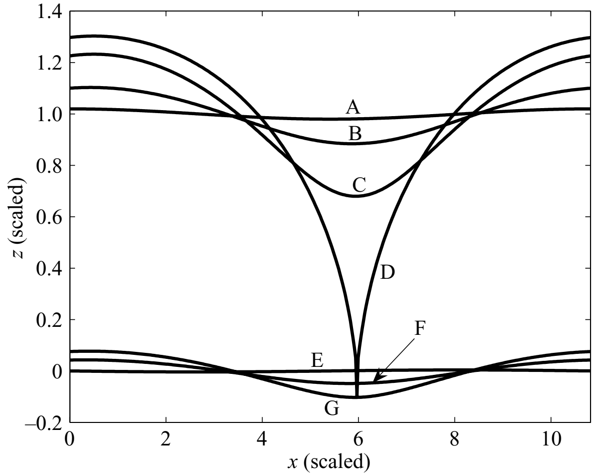

FIGURE 13. Evolution of mode with a $\pi/2$ phase shift, with otherwise the same initial conditions as figure 11. Symmetry is broken by the phase shift of the CM interface. The curves for the MG interface are labelled A–D, at times $\hat{\tau} = 0$, $\hat{\tau} = 9.3$, $\hat{\tau} = 14.7$ and $\hat{\tau} = 16.5$, respectively. Curves for the CM interface are labelled E–G, at times $\hat{\tau} = 0$, $\hat{\tau} = 12.9$ and $\hat{\tau} = 16.5$, respectively. Again, the tip accelerates as it approaches the approximate rupture time of $\hat{\tau}_R = 16.5$.

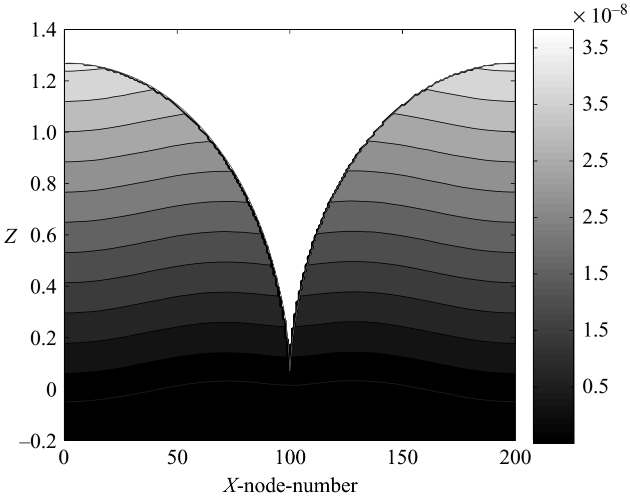

FIGURE 14. Temperature field at a time near rupture. Scaled temperature decreases as the grey scale darkens.

7.2. *Nonlinear oscillatory interface evolution*

Initial conditions from regions III and IV of the stability diagram (figure 5) result in oscillatory behaviour. For an initially symmetric configuration, the rupture occurs by growth of a standing wave. Such oscillatory dynamics are illustrated in figure 15, in which midpoints of both MG and CM surfaces are plotted as a function of scaled time. The system is started in the pinch mode with an initial amplitude of $A = 0.01$ on the melt–gas interface and rupture occurs at $\hat{\tau} \approx 63$. As the system evolves, a phase shift develops in which oscillation of the CM interface lags behind the MG interface. This indicates a difference in the dynamic time scale of the melting/freezing process at the CM interface as compared to the dynamics of the MG interface.

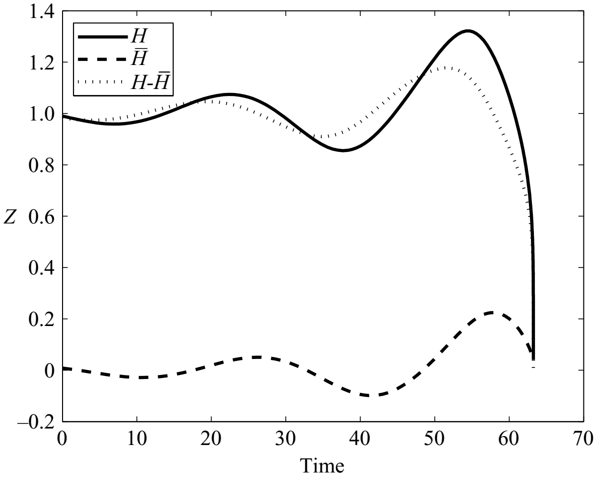

FIGURE 15. Time evolution of the rupture point position. The amplitude of oscillation increases and the film eventually ruptures once a critical separation between H and $\overline{H}$ has been reached. The solid line is the MG interface H, the dashed line is the CM interface $\overline{H}$, and the dotted line is the difference $H-\overline{H}$.

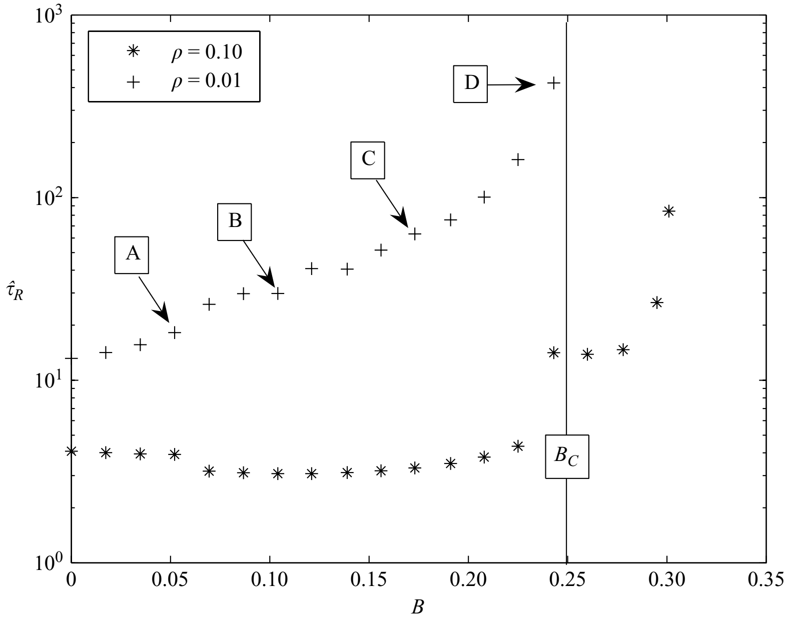

FIGURE 16. Rupture time varies as B increases. Amplitude of the initial perturbation is 0.1 for the '*' curve, and 0.01 for the '+' curve. B_C is the critical value of the parameter B denoting the onset of instability. The steps are a result of a change in the number of oscillation periods before rupturing, as shown in the phase plane plots in figure 17. The letters A–D correspond to the points selected for the phase plane plots.

Figure 16 provides a summary of the effect of oscillatory behaviour on rupture dynamics as B is increased from zero to the critical temperature B_C, which is at the peak of the marginal stability curve. The wavenumber at the maximum of the (B, ω) marginal stability surface is used in all calculations, as this is the maximum growth

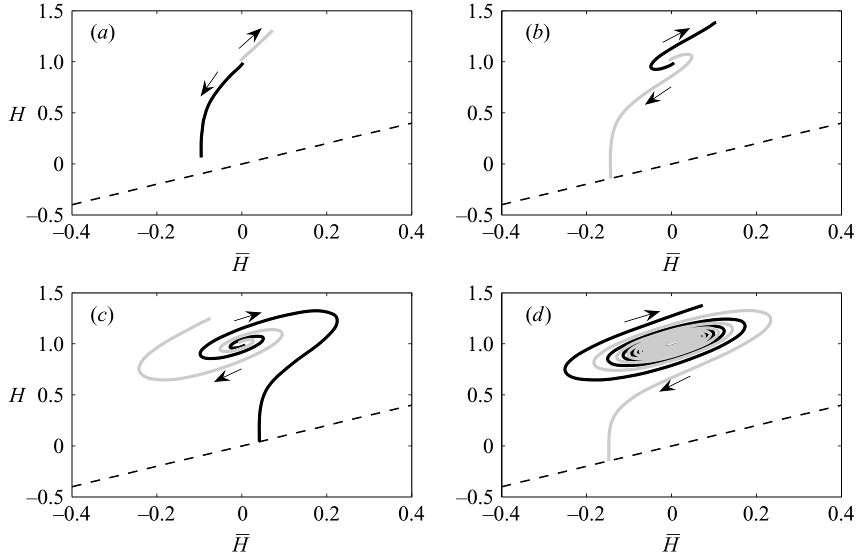

FIGURE 17. Series of phase plane plots of H versus $\overline{H}$. The solid curves give the surface midpoint locations and the light curves are the surface endpoint locations. The dashed line gives the positions where $H=\overline{H}$. Plots (*a*)–(*d*) correspond to points A–D in figure 16. (*a*) corresponds to stationary rupture, in which the solid curve reaches the $H=\overline{H}$ line. (*b*) is the second half-integer oscillatory rupture. (*c*) and (*d*) show increasing numbers of oscillations before rupture, as the thermal parameter approaches the marginal stability criteria.

rate for all B. According to linear theory, $\hat{\tau}_R$ should go to infinity as B approaches B_C. The curve described by the '+' symbols in figure 16 corresponds to a small, $A=0.01$, initial perturbation amplitude and does tend towards an infinite $\hat{\tau}_R$ at B_C, in agreement with the limit imposed by linear theory. Larger initial perturbations given by the '*' symbols, however, are unstable for values of B greater than B_C, a nonlinear finite amplitude effect. The step-like features exhibited in both curves as B increases correspond to increases in half-integer number of oscillation periods before rupture. Figure 17 presents a series of phase plane plots of H versus $\overline{H}$ at the four values of B indicated in figure 16. The phase plane plots are all taken from identical initial shape configurations and show how oscillations affect time to rupture. At A there is no oscillation, at B there is the second one-half oscillation before rupture, and C and D show the cases for many oscillations.

Additional insight is gained by examining the temperature gradient which is shown in figure 18 as a sequence of snapshots of a film and the thermal gradient within, on the way to rupture via the growth of a standing wave. The light areas correspond to the location of maximum temperature gradient and it is seen that the maximum temperature gradient is always aligned with the narrowest region of the film, since heat flow is quasi-static. This figure supports a mechanism of stabilization and oscillation of the film by means of a thermal field directly opposing the destabilizing van der Waals attractive forces.

8. Conclusions

A novel, governing pair of nonlinear equations is derived for the crystal–melt and melt–gas interfaces bounding a melt film, by utilizing lubrication theory and

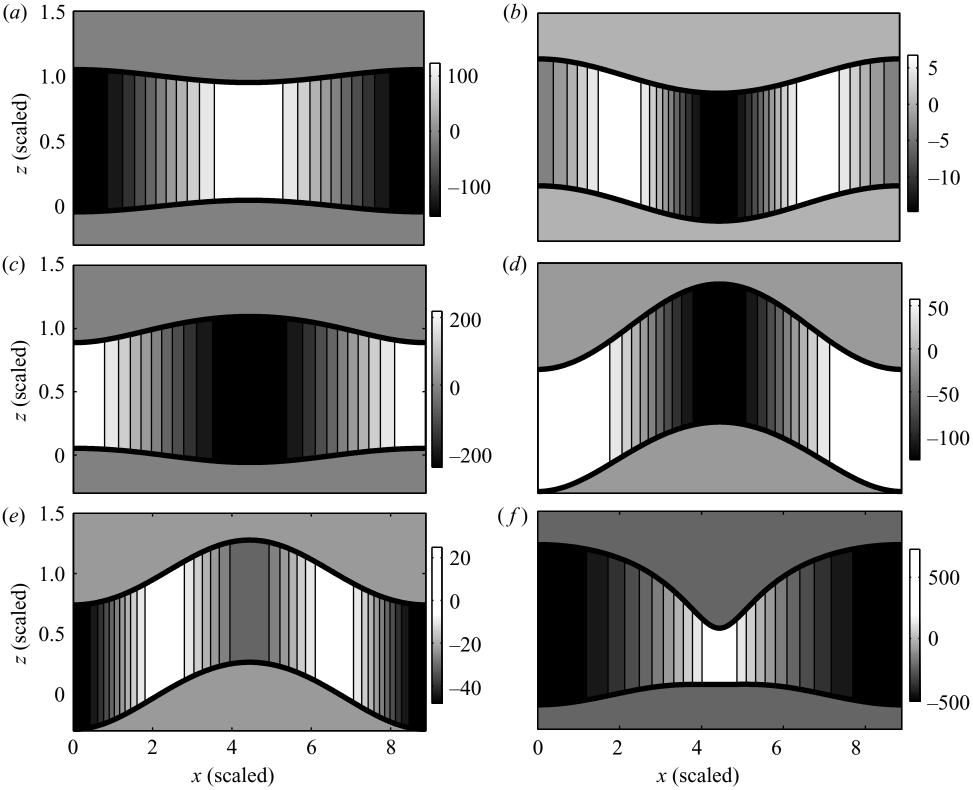

FIGURE 18. Temperature gradient sequence with subplots (*a*)–(*f*) corresponding to scaled times $\hat{t} = 0, 9.78, 14.61, 23.41, 24.51$ and 29.67, respectively. Note that the temperature gradient scale-bar range increases as the separation between the surfaces decreases. Additionally, the maximum gradient always occurs at the location of minimum separation. The MG and CM interfaces were discretized with 800 spatial nodes.

long-wave dynamics. Linear stability analysis of the thin film reveals that, when an applied thermal field and a crystal–melt interface evolving by freezing/melting is coupled with the van der Waals forces and melt–gas interface capillary effects, oscillatory instability at *all* marginally stable conditions is observed (i.e. wherever σ_r vanishes). Key practical findings of this work are that an increase in the temperature gradient in a transverse direction across the thin film *stabilizes* the thin film and, as the magnitude of the temperature gradient across a stable film is decreased, one would observe the onset of instability as a disturbance having a particular wavelength. Eigenfunctions of the linear theory show a transition of the thermal field from in-phase to out-of-phase alignment with respect to the gas–melt interface as the temperature gradient is increased, leading to oscillatory behaviour.

Numerical analysis of the fully nonlinear pair of governing equations shows that, for stationary instabilities, as the upper MG interface nears the rupture point at the lower CM interface, the lower interface retreats by melting back. Since the film is very narrow, thermal diffusion is unidirectional and quasi-static. Therefore, near the rupture tip, both the van der Waals forces and the heat flux are largest, and so as the rupture tip is approaching the crystal–melt interface, a larger amount of heat is being fed to the CM interface in this region compared to adjacent regions. This heat is consumed at the crystal–melt interface as latent heat, promoting local melting. Small (linear) symmetric perturbations are shown to grow to rupture as standing waves, and with increasing number of oscillations, the closer the initial configuration is to the marginal stability condition. For larger initial shape perturbations, the region on a plot of the thermal parameter $B=\overline{C}^{-1}Bi^2\Theta_\infty/(3\hat{\hat{L}}\tilde{A}^2(1+Bi)^2)$ (a measure of the magnitude of the positive temperature gradient across the melt) versus the wavenumber ω, within which perturbations can grow to rupture, increases, whereas the time to rupture decreases.

Discussions with S. H. Davis, A. A. Golovin, L. Fisher and S. Roper are appreciated.

REFERENCES

Ajaev, V. S. & Willis, D. A. 2006 Heat transfer, phase change, and thermocapillary flow in films of molten metal on a substrate. *Numer. Heat Transfer* A **50**, 301–313.

Anson, J. P., Drew, R. A. L. & Gruzleski, J. E. 1999 The surface tension of molten aluminum and Ag-Si-Mg alloy under vacuum and hydrogen atmospheres. *Metall. Mater. Trans.* B **30**, 1027–1032.

Ashby, M. F., Evans, A. G., Fleck, N. A., Gibson, L. J., Hutchinson, J. W. & Wadley, H. N. G. 2000 *Metal Foams: A Design Guide*. Butterworth–Heinemann.

Bandyopadhyay, D., Gulabani R. & Sharma A. 2005 Instability and dynamics of thin liquid bilayers. *Indust. Engng Chem. Res.* **44**, 1259–1272.

Banhart, J. 2001 Manufacture, characterization and application of cellular metals and metal foams. *Prog. Mater. Sci.* **46**, 559–632.

Burelbach, J., Bankoff, S. & Davis, S. 1988 Nonlinear stability of evaporating/condensing liquid films. *J. Fluid Mech.* **195**, 463–494.

Chernov, A. A. & Temkin, D. E. 1976 Capture of inclusions in crystal growth. In *Current Topics in Materials Science*, Vol. 2 (ed. E. Kaldis), pp. 3–77. North-Holland.

Dash, J., Fu, H. & Wettlaufer, J. 1995 The premelting of ice and its environmental consequences. *Rep. Prog. Phys.* **58**, 115–167.

Davis, S. H. 2000 Interfacial fluid dynamics. In *Perspectives in Fluid Dynamics* (ed. G. K. Batchelor, H. K. Moffatt & M. G. Worster), pp. 1–49. Cambridge University Press.

Dinsdale, A. T. & Quested, P. N. 1999 The viscosity of aluminium and its alloys: A review of data and models. *J. Materials Sci.* **39**, 7221–7228.

Erneaux, T. & Davis, S. H. 1992 Nonlinear rupture of free films. *Phys. Fluids* **5**, 1117–1122.

Fisher, L. S. & Golovin, A. A. 2005 Nonlinear stability analysis of a two layer thin liquid film: Dewetting and autophobic behavior. *J. Colloid Interface Sci.* **291**, 515–528.

Frenken, J. W .M. & van der Veen, J. F. 1985 Observation of surface melting. *Phys. Rev. Lett.* **54**, 134–137.

Hur, B. Y., Park, S. H. & Hiroshi, A. 1989 Viscosity and surface tension of Al and effects of additional element. In *Eco-Materials Processing and Design, Mater. Sci. Forum* **439**, 51–56.

Israelachvili, J. N. 1991 *Intermolecular and Surface Forces*. Academic.

Kao, J. C.-T., Golovin, A. A. & Davis, S. H. 2006 Rupture of thin films with resonant substrate patterning. *J. Colloid Interface Sci.* **303**, 532–545.

Oron, A., Davis, S. & Bankoff S. 1997 Long scale evolution of thin liquid films. *Rev. Mod. Phys.* **69**, 931–980.

Pluis, B., van der Gon, A. D., Frenken, J. & van der Veen, J. 1987 Crystal-face-dependence of surface melting. *Phys. Rev. Lett.* **59**, 2678–2681.

Pluis, B., Taylor, T .N., Frenkel, D. & van der Veen, J. F. 1989 Role of long range interactions in the melting of a metallic surface. *Phys. Rev.* B **40**, 1353–1356.

Ruckenstein, E. & Jain R. 1974 Spontaneous rupture of thin liquid films. *Chem. Soc. Faraday Trans.* **70**, 132–147.

Shampine, L. F. & Reichelt, M. W. 1997 The MATLAB ode suite. *SIAM J. Sci. Comput.* **18**, 1–22.

Sheludko, A. 1967 Thin liquid films. *Adv. Colloid Interface Sci.* **1**, 391–463.

Tartaglino, U., Zykova-Timan, T., Ercolesi, F. & Tosatti, E. 2005 Melting and non-melting of solid surfaces and nanosystems. *Phys. Rep.* **411**, 291–321.

VanHook, S. J., Schatz, M. F., McCormick, W. D., Swift, J. B. & Swinney, H. L. 1995 Long-wavelength instability in surface-tension driven Bénard convection. *Phys. Rev. Lett.* **75**, 4397–4400.

Weaire, D. & Hutzler, S. 1999 *The Physics of Foam.* Oxford University Press.

Wettlaufer, J. S. & Worster, M. G. 2006 Premelting dynamics. *Annu. Rev. Fluid Mech.* **38**, 427–452.

Wettlaufer, J., Worster, M. G., Wilen, L. A. & Dash, J. G. 1996 A theory of premelting dynamics for all power law forces. *Phys. Rev. Lett.* **76**, 3602–3605.

Wettlaufer, J., Worster, M. G. & Wilen, L. 1997 Premelting dynamics: Geometry and interactions. *J. Phys. Chem.* B **101**, 6137–6141.

Wheeler, A .A. 1993 *Handbook of Crystal Growth*, Vol. 1. Elsevier.

Wilen, L. A, Wettlaufer, J. S., Elbaum, M. & Schick, M. 1995 Dispersion-force effects in interfacial premelting of ice. *Phys. Rev.* B **52**, 12426–12433.

Williams, M. & Davis, S. H. 1982 Nonlinear theory of film rupture. *J. Colloids Interface Sci.* **90**, 220–228.

Wu, Q. & Wong, H. 2004 A slope-dependent disjoining pressure for non-zero contact angles. *J. Fluid Mech.* **506**, 157–185.

Zhang, W. W. & Lister, J. R. 1999 Similarity solutions for the van der Waals rupture of a thin film on a solid substrate. *Phys. Fluids* **11**, 2454–2462.